



# Suppression of instabilities of swirled premixed flames with minimal secondary hydrogen injection

Gorkem Oztarlik, Laurent Selle, Thierry Poinso, Thierry Schuller

## ► To cite this version:

Gorkem Oztarlik, Laurent Selle, Thierry Poinso, Thierry Schuller. Suppression of instabilities of swirled premixed flames with minimal secondary hydrogen injection. *Combustion and Flame*, 2020, 214, pp.266-276. 10.1016/j.combustflame.2019.12.032 . hal-02538681

**HAL Id: hal-02538681**

**<https://hal.science/hal-02538681>**

Submitted on 9 Apr 2020

**HAL** is a multi-disciplinary open access archive for the deposit and dissemination of scientific research documents, whether they are published or not. The documents may come from teaching and research institutions in France or abroad, or from public or private research centers.

L'archive ouverte pluridisciplinaire **HAL**, est destinée au dépôt et à la diffusion de documents scientifiques de niveau recherche, publiés ou non, émanant des établissements d'enseignement et de recherche français ou étrangers, des laboratoires publics ou privés.



## Open Archive Toulouse Archive Ouverte





OATAO is an open access repository that collects the work of Toulouse researchers and makes it freely available over the web where possible

This is an author's version published in: <http://oatao.univ-toulouse.fr/25707>

### Official URL:

<https://doi.org/10.1016/j.combustflame.2019.12.032>

### To cite this version:

Oztarlik, Gorkem  and Selle, Laurent  and Poinso, Thierry   
and Schuller, Thierry  *Suppression of instabilities of swirled  
premixed flames with minimal secondary hydrogen injection.*  
(2020) Combustion and Flame, 214. 266-276. ISSN 0010-2180.

Any correspondence concerning this service should be sent  
to the repository administrator: [tech-oatao@listes-diff.inp-toulouse.fr](mailto:tech-oatao@listes-diff.inp-toulouse.fr)

# Suppression of instabilities of swirled premixed flames with minimal secondary hydrogen injection

Gorkem Oztarlik, Laurent Selle, Thierry Poinso, Thierry Schuller\*

*Institut de Mécanique des Fluides de Toulouse, IMFT, Université de Toulouse, CNRS, Toulouse, France*

## A B S T R A C T

The impact of hydrogen addition on the dynamics of a methane-air premixed flame is explored for different injection strategies. The configuration is a swirled injector with a central tube for pilot fuel injection. Keeping the air flow rate and thermal power of the burner constant, it is shown that even for very small flow rates of hydrogen, as low as one percent of the thermal power, flame stabilization and combustor stability are greatly altered when pure hydrogen is injected through the central tube as a pilot jet. It is also shown that fully premixing the same quantity of hydrogen with methane or use of methane for the pilot jet has no significant effects compared to hydrogen pilot injection strategy. The flame response to forced flow perturbations is used to interpret the observed features. It is shown that hydrogen piloting drastically changes the gain of the flame transfer function at low frequencies and its phase lag at high frequencies, while other injection strategies barely change the flame response for these minute flowrates. CO and NO<sub>x</sub> emissions are finally examined for the different injection strategies. NO<sub>x</sub> emissions are found to drastically increase with hydrogen piloting compared to other injection strategies. These experiments indicate that pure hydrogen injected in minute fractions may be used as an efficient passive control means to mitigate combustion instabilities, but a compromise needs to be made with emissions.

## 1. Introduction

Gas turbines fired with natural gas is one the most efficient solution for power generation with limited pollutant emissions and reduced carbon dioxide emissions, compared to other power generation units burning hydrocarbon fuels [1–3]. Typical industrial gas turbines operate on natural gas in a lean premixed regime to cut down NO<sub>x</sub> emissions, but these systems suffer from dynamical problems mainly associated to combustion instabilities [4]. Instances of heat shields breaking due to high cycle fatigue, damaged burners, liners and transition pieces are regularly reported [5]. With the introduction of new gases from renewable sources in the fuel supply line, such as biogas or syngas, these issues become more critical due to (1) changes in the fuel composition powering the engine and altering the heat release distribution for a given thermal power output [6–9] and (2) intermittent changes of the supply and power demand leading to operation with high turn-down ratios [10].

Blending hydrogen from renewable sources into natural gas can be used to reduce carbon dioxide emissions without impairing

pollutant emissions. In this strategy, hydrogen is premixed with natural gas prior to combustion. But it was found out that although hydrogen addition widens the static operability range of the combustor by improving blow-off characteristics, it tends to make combustion systems more prone to flashback and more sensitive to combustion instabilities even at low power regimes and more quickly compared to natural gas [11–15].

An alternative way to avoid flashback issues and mitigate combustion instabilities is to use a pilot fuel circuit, burning a fraction of the fuel in partially premixed or non-premixed mode, while the main fuel stage burns in a lean premixture. This strategy helps achieving more stable flames [16–19] and has also been proven on full scale engine tests [20,21]. Because hydrogen has a higher extinction strain rate compared to methane and natural gas, it is a good candidate to serve as a pilot fuel.

The use of a hydrogen pilot fuel jet has been considered in a few studies. Hussain et al. [22] recently made a clear review of these studies in their introduction. In one of the pioneering works, Anderson et al. [23] noted that it would make flames quieter and more stable in a perforated-plate flame holder configuration. More recently, Barbosa et al. [24] showed that a swirled injection of hydrogen into a combustor operated with a lean propane-air mixture can be used to reduce combustion oscillations, without impairing NO<sub>x</sub> emissions but with a drastic increase in CO

\* Corresponding author.

E-mail address: [thierry.schuller@imft.fr](mailto:thierry.schuller@imft.fr) (T. Schuller).

emissions. Hussain et al. [22] analyzed the response to acoustic perturbations of methane-air and ethylene-air flames stabilized by a large bluff body in a dump combustor, when secondary hydrogen is injected through the bluff body. They found that the Flame Describing Function (FDF) linking the acoustic velocity modulation to the resulting heat release rate oscillation at 30, 255 and 315 Hz could be lowered compared to operation without hydrogen for all acoustic forcing levels tested. However, NOx emissions rapidly increase when the hydrogen concentration exceeds 5% in volume. Their analysis carried out without swirl is also limited to selected forcing frequencies.

In this study, an experimental setup with separate injection of hydrogen is considered with the objective to alter the dynamic stability of a swirled combustor operated with methane, used here as a surrogate for natural gas. The fraction of hydrogen injected in the system is kept very low to limit NOx emissions. The goal is to change the distribution of heat release in order to affect flame stabilization and its dynamics without altering the global thermal power and the air flow rate through the system. The effectiveness of this strategy is compared by replacing hydrogen with methane for the pilot fuel or by fully premixing methane and hydrogen in order to discriminate between the effects of fuel composition and injection strategies. The flame response to acoustic perturbations is then analyzed for these different injection strategies. Use of the burner impedance and Flame Transfer Function (FTF) is finally made to identify the mechanisms through which the combustor stability is affected.

This paper is organized as follows. First some generic definitions and theoretical considerations about hydrogen-enriched combustion are given in Section 2. The experimental setup and diagnostics are then presented in Section 3, followed by a detailed comparison of stability maps in Section 4 for the various fuel injection configurations. A deeper analysis of one selected unstable operating point is finally conducted in Section 5 through the scrutiny of pressure traces, flame visualisations and FTF. Pollutant emissions are finally examined in Section 6 for the different injection strategies.

## 2. Definitions for hydrogen-enriched systems

When multiple fuels are used simultaneously, care is required for a consistent definition of basic combustion parameters. Whether the fuels are premixed or injected separately, one may define the molar fraction of each species in the hypothetical fuel mixture. In this study considering hydrogen and methane, the molar fraction of hydrogen in the fuel is:

$$X_{H_2}^f = \frac{\dot{n}_{H_2}}{\dot{n}_{H_2} + \dot{n}_{CH_4}} \quad (1)$$

where  $\dot{n}_j$  denotes the molar flow rate of species  $j$ . Then, the balance equation for lean combustion of this multicomponent fuel may be written:

$$\begin{aligned} \phi_G (X_{CH_4}^f CH_4 + X_{H_2}^f H_2) + \left(2 - \frac{3}{2} X_{H_2}^f\right) (O_2 + a N_2) \\ \rightarrow \phi_G (X_{CH_4}^f CO_2 + (2 - X_{H_2}^f) H_2O) \\ + \left(2 - \frac{3}{2} X_{H_2}^f\right) ((1 - \phi_G) O_2 + a N_2) \end{aligned} \quad (2)$$

where  $a = 3.76$  is the molar fraction of nitrogen in air and  $X_{CH_4}^f = 1 - X_{H_2}^f$  is the molar fraction of methane in the fuel blend. The global equivalence ratio is defined as  $\phi_G = \alpha / \alpha_s$ , where  $\alpha = \dot{m}_f / \dot{m}_a$  is the ratio between the fuel and air mass flow rates injected in the burner. The stoichiometric value of  $\alpha$  is:

$$\alpha_s = \frac{X_{CH_4}^f W_{CH_4} + X_{H_2}^f W_{H_2}}{\left(2 - \frac{3}{2} X_{H_2}^f\right) (W_{O_2} + a W_{N_2})} \quad (3)$$

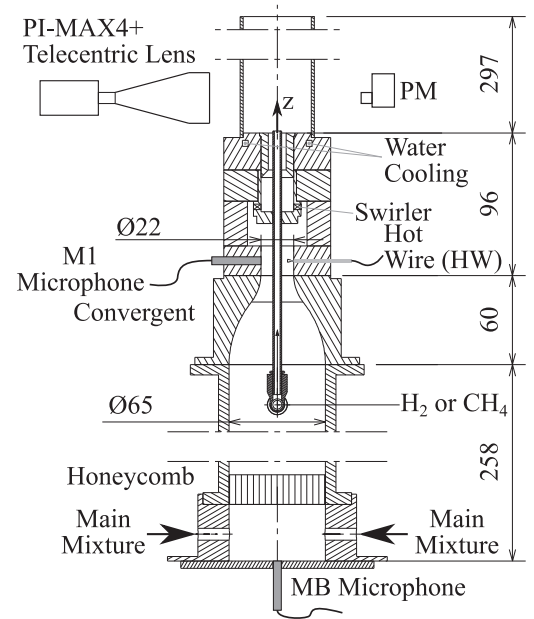


Fig. 1. Schematic representation and relevant dimensions of the experimental setup. Dimensions are in millimeters.

where  $W_j$  is the molar mass of species  $j$ . Finally, for the analysis conducted in this paper, it is relevant to define the fraction of the total thermal power  $\mathcal{P}_{H_2}$  attributed to hydrogen combustion:

$$\mathcal{P}_{H_2} = \frac{X_{H_2}^f Q_{H_2}}{X_{H_2}^f Q_{H_2} + X_{CH_4}^f Q_{CH_4}} \quad (4)$$

where  $Q_j$  is the molar lower heating value of species  $j$ .

## 3. Experimental setup and diagnostics

The objective of the study is to alter the dynamics of a burner equipped with a radial swirling vane with the addition of hydrogen. Therefore, the configuration that is presented in Fig. 1 consists of a swirled injector fed with a gaseous mixture, plugged into a cylindrical flame tube. This burner is an evolution of that used in [25–27] operating in fully premixed mode. Here the central insert is replaced by a pilot fuel line aligned with the swirler axis.

The main mixture of fuel and air is injected at the bottom of a plenum with a circular cross section of diameter  $D_p = 65$  mm. The acoustic pressure is recorded at the bottom of the plenum via a Brüel & Kjær-TYPE 4954 microphone (MB) and a honeycomb panel is fitted in the plenum to break the turbulent structures resulting from the injection. Two plenum lengths  $l_p = 258$  mm and  $l_p = 147$  mm are available to modify the acoustic response of the setup.

The flow then goes through a convergent nozzle that ensures a laminar flow with less than 1% velocity fluctuation with a top hat velocity profile, followed by a short annular tube of diameter  $D = 22$  mm. In this tube, the acoustic pressure and the velocity are recorded with microphone M1 flush mounted to the wall and a constant temperature anemometer (Dantec 55P16 miniature hot wire probe and a Dantec 54T42 MiniCTA), denoted HW. The microphone M1 and the hot wire probe HW are located in the same section in front of each other as shown in Fig. 1. This section is designated in the following by section (1). Care has been taken to set the hot wire probe outside of the boundary layer, where the velocity is uniform with a top hat velocity profile.

Then follows a radial swirler with 8 feed channels of 4.5 mm diameter each, which are  $15^\circ$  off the swirler axis. The flow leaves

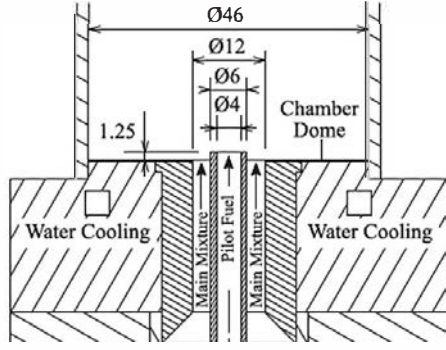


Fig. 2. Detailed view of the injection system with the main dimensions are in millimeters.

the swirler through the main annular injection channel with a reduced external diameter of 12 mm to avoid flashback. A detailed view of this component is given in Fig. 2, together with its main dimensions.

The bulk velocity  $U_{sw}$  that is used to define the operating conditions is determined in the main mixture annular injection channel at temperature  $T_u = 292$  K. It has a cross section area  $A = 84.82$  mm<sup>2</sup> with 6 mm internal diameter and 12 mm external diameter. The swirl number determined from numerical flow simulations is  $S_w = 0.4$  at the injector outlet. The top of the burner is water cooled in order to maintain the thermal equilibrium of the plenum at room temperature,  $T_u = 292$  K. The outlet of the annular injection channel defines section (0) of the burner at altitude  $z = 0$ . The piloting system consists of a central stainless steel tube with a 6 mm external diameter and a 4 mm internal diameter, aligned with the burner axis where pure fuel can be injected. The tube protrudes  $z = 1.25$  mm inside the combustion chamber to ease flame visualization at its base when the flame is anchored at this location. The combustion chamber consists of cylindrical quartz tubes with an internal diameter of 46 mm. Two flame tube lengths are available,  $l_f = 300$  mm and  $l_f = 100$  mm, the smaller being used for the measurement of flame responses to acoustic perturbations as described in Section 5.3.

The mass flow rates of methane, air and hydrogen are controlled separately (Brooks SLA 585x series), so that the fraction of the thermal power from hydrogen  $\mathcal{P}_{H_2}$  can be regulated as well as the global equivalence ratio  $\phi_G$ . Hydrogen can be added in the main mixture to operate in fully premixed mode or through the pilot tube. Methane can also be used as the pilot fuel for comparison, meaning that this system is versatile for the development of control strategies via fuel composition and injection.

Heat release rate fluctuations of the flame are deduced from the emission intensity of  $CH^*$  radicals. They are recorded with a photomultiplier along with a band-pass filter centered on the  $CH^*$  emission spectrum peak  $\lambda = 430 \pm 10$  nm (THORLABS FB430-10). Flame images are also taken with a camera (PI-MAX4) along

Table 1  
Operating conditions.

Case	Main		Pilot		$\mathcal{P}_{main}$ [%]	$\mathcal{P}_{pilot}$ [%]	$\mathcal{P}_{H_2}$ [%]
	$X_{H_2}^f$ [%]	$X_{CH_4}^f$ [%]	$X_{H_2}^f$ [%]	$X_{CH_4}^f$ [%]			
Ref	0.0	100.0	0.0	0.0	100.0	0.0	0.0
PC1	0.0	99.0	0.0	1.0	99.0	1.0	0.0
PC2	0.0	98.0	0.0	2.0	98.0	2.0	0.0
PH1	0.0	96.8	3.3	0.0	99.0	1.0	1.0
PH2	0.0	93.7	6.6	0.0	98.0	2.0	2.0
MH1	3.3	96.8	0.0	0.0	100.0	0.0	1.0
MH2	6.6	93.7	0.0	0.0	100.0	0.0	2.0

with an appropriate filter (ASAHI XHQA430) also centered on  $\lambda = 430 \pm 10$  nm and a telecentric lens (Opto Engineering TC4M120), which provide valuable information on the shape and heat release distribution of the flame. The telecentric lens avoids image distortion due to perspective effects compared to classical lenses.

The experiments presented in this paper are conducted at lean operating conditions,  $0.70 \leq \phi_G \leq 0.85$ , and for bulk flow velocities,  $14 \text{ m.s}^{-1} \leq U_{sw} \leq 40 \text{ m.s}^{-1}$ , corresponding to thermal powers in the range  $2700 \text{ W} \leq \mathcal{P} \leq 9300 \text{ W}$ . Gases are injected in the setup at room temperature  $T_u = 292$  K. These conditions correspond to injection Reynolds numbers  $5541 \leq Re_{D_h} \leq 15831$  based on the hydraulic diameter  $D_h = 6$  mm of the main annular injection channel (Fig. 2).

#### 4. Stability maps

The dynamic stability of the combustor is examined for the operating range given in Section 3. In order to evaluate the effect of hydrogen on the stability of each operating point, different injection strategies are tested as illustrated in Fig. 3. These variations are conducted at constant thermal power  $\mathcal{P}$  because this parameter has a first-order impact on the magnitude of combustion instabilities. Therefore, the control parameters are the fraction of the thermal power from hydrogen,  $\mathcal{P}_{H_2}$  and that from the pilot flame,  $\mathcal{P}_{pilot}$ . Accordingly, the fraction of power from the main mixture is  $\mathcal{P}_{main} = 1 - \mathcal{P}_{pilot}$ . The reference is a fully premixed methane-air case without piloting, labelled 'Ref' in Fig. 3. Then piloting with hydrogen is considered in cases PH1 and PH2 corresponding to  $\mathcal{P}_{H_2} = 1\%$  and  $2\%$ , respectively. Cases PC1 and PC2 correspond to the replacement of hydrogen by methane in the pilot tube, with the same levels of power  $\mathcal{P}_{pilot}$ . Finally, in cases MH1 and MH2 the pilot is turned off and the hydrogen is premixed in the main stream, with corresponding power fractions  $\mathcal{P}_{H_2}$ . All these cases are summarized in Table 1. They allow a systematic investigation of effects of fuel composition, injection strategy and pilot fuel at low levels of hydrogen addition. These experiments are conducted with a long flame tube,  $l_f = 300$  mm and a long plenum  $l_p = 221$  mm (see Fig. 1).

The stability map of the reference case is presented in Fig. 4. It shows the evolution of the magnitude of pressure fluctuations

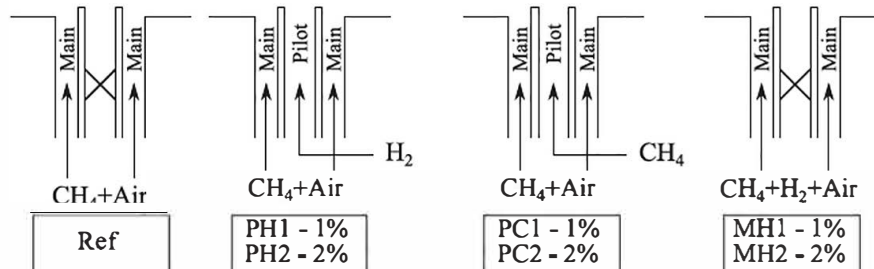


Fig. 3. Representation of the injection strategies that are tested. The cross indicates that the pilot fuel stage is not used.



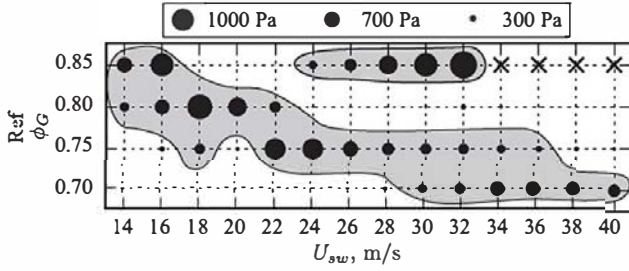


Fig. 4. Stability map of the methane-air fully premixed flame. Case Ref in Table 1 and Fig. 3. Root-mean-square fluctuations of pressure at MB versus bulk velocity  $U_{sw}$  and equivalence ratio  $\phi_G$ .

recorded by the microphone MB for variations in bulk velocity  $U_{sw}$  and equivalence ratio  $\phi_G$ . The radii of the disks in Fig. 4 are proportional to the root-mean-square (RMS) value of the pressure fluctuations measured by microphone MB. The grey shaded regions delineate the regions of instability, defined here as the operating conditions where RMS pressure fluctuations are higher than 300 Pa. This threshold level was chosen as representative of established self-sustained combustion oscillations associated to a coherent peak in the recorded power spectra. Variations of this threshold show similar results even though the boundaries of the unstable regions are slightly shifted. For some operating conditions, hysteresis takes place in which cases the instability jumps from one intensity to another. These operating conditions are marked with half circles. Finally, a X indicates a condition that was not explored because the instability is too strong and may damage the burner. This nomenclature is used for Figs. 4 through 7. Figure 4 shows that the reference configuration exhibits two regions of instability, one at  $\phi_G=0.85$  for flow velocities higher than  $U_{sw} \geq 24 \text{ m.s}^{-1}$  ( $Re_{D_h} \geq 9500$ ) and another one along the descending diagonal covering a large fraction of the operational domain. The peak frequency of these self-sustained modes lies between 520 Hz and 680 Hz depending on the operating point considered.

The control strategy that is explored is the pilot injection of hydrogen in small quantities. For PH1 (respectively PH2), 1% (respectively 2%) of the methane flow rate is removed from the main mixture and the hydrogen pilot flow rate is adjusted to compensate for the loss in thermal power. Because of the large differences in molecular weight between  $H_2$  and  $CH_4$ , this yields a molar fraction of hydrogen in the total fuel flow  $X_{H_2}^f = 3.3\%$  for PH1 and  $X_{H_2}^f = 6.6\%$  for PH2 (see Table 1). The corresponding stability maps are shown in Fig. 5. Markers  $\diamond$  correspond to operating conditions that could not be explored because the pilot mass flow rates are too small for a stable regulation by the mass-flow controllers. The peak frequency of the unstable modes lies close to those found for the same bulk flow velocity and equivalence ratio in the Ref stability map.

For PH1 there is a reduction of the acoustic pressure level in the system for velocities in the range  $18 \text{ m.s}^{-1} \leq U_{sw} \leq 28 \text{ m.s}^{-1}$  and the total number of unstable points has been reduced by one third. This is a very significant impact of the hydrogen injection for it contributes to only 1% of the thermal power. A further increase in the hydrogen content (case PH2 in Fig. 5) results in the complete suppression of all unstable points for  $U_{sw} \leq 24 \text{ m.s}^{-1}$  and  $\phi_G=0.7$ . The conclusion is that a minimal level of hydrogen piloting has allowed to stabilize the unstable operating points at low thermal power. However, the stability of the combustor at high power, i.e. the upper-right quadrant in Fig. 5, gets worse as the pilot hydrogen is increased. Interestingly, in these conditions, the bulk flow velocity  $U_{H_2}$  of the hydrogen flow in the pilot tube is less than 3% of the bulk velocity  $U_{sw}$  of the swirled flow in the main annular in-

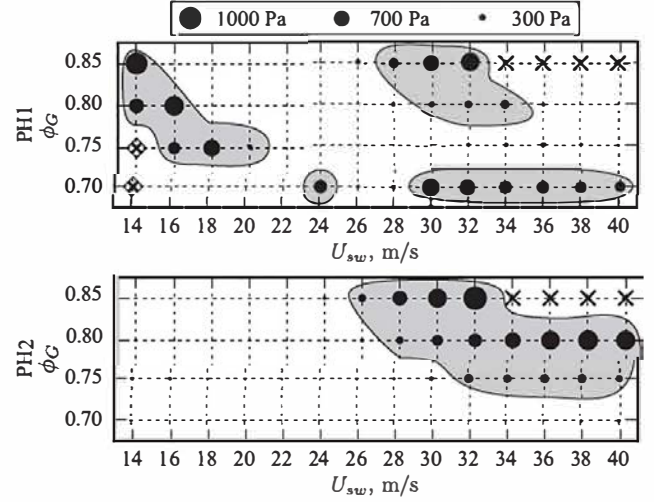


Fig. 5. Stability maps of the configurations with hydrogen pilot injection. Cases PH1 and PH2 in Table 1 and Fig. 3. Root-mean-square fluctuations of pressure at MB versus bulk velocity  $U_{sw}$  and equivalence ratio  $\phi_G$ .

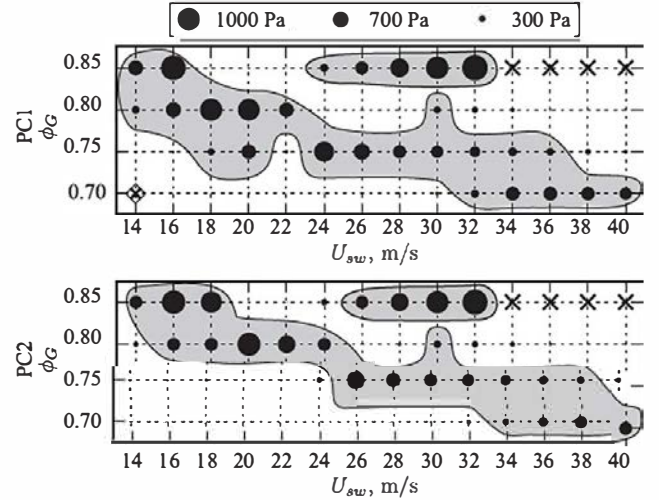


Fig. 6. Stability maps of the configurations with methane pilot injection. Cases PC1 and PC2 in Table 1 and Fig. 3. Root-mean-square fluctuations of pressure at MB versus bulk velocity  $U_{sw}$  and equivalence ratio  $\phi_G$ .

jection channel. This rules out that direct modifications of the flow field caused by the pilot jet would be the cause for the modified stability.

In order to mimic a practical situation, it was chosen to keep the air flow rate and the thermal power constant. Therefore, hydrogen piloting yields small changes in global equivalence ratio  $\phi_G$  and bulk velocity  $U_{sw}$  in the main annular injection channel. One can show that for PH1 (respectively PH2),  $U_{sw}$  is reduced to 99.9% (respectively 99.8%) of the bulk velocity of case Ref. The reduction of  $\phi_G$  is less than 0.1% so that these differences are neglected in the present study.

It is well known that fuel piloting affects the stability of swirl burners. In order to assess the influence of hydrogen, methane piloting is considered with cases PC1 and PC2, by replacing  $H_2$  with  $CH_4$ . The corresponding stability maps are shown in Fig. 6. The comparison with the reference case in Fig. 4 indicates that the stability is marginally impacted, even for case PC2, which has the largest methane pilot flowrate.

The two cases with pilot injection suggest that the change in the global composition of the fuel, namely hydrogen addition, is the driving factor for the improved stability. A third set of cases is

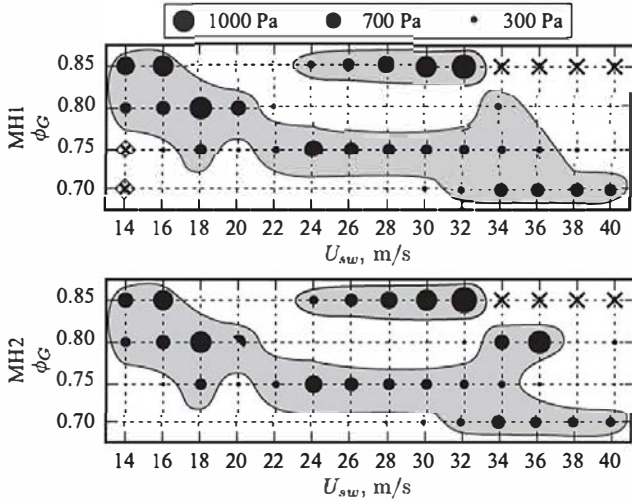


Fig. 7. Stability maps of configurations with the hydrogen-enriched methane/air mixtures. Cases MH1 and MH2 in Table 1 and Fig. 3. Root-mean-square fluctuations of pressure at MB versus bulk velocity  $U_{sw}$  and equivalence ratio  $\phi_G$ .

devised where the hydrogen content is identical to piloting cases, but fully premixed within the main injection stream. In MH1 and MH2, the pilot is closed and the hydrogen is premixed with the methane and air, and sent through the swirler. The corresponding stability maps are presented in Fig. 7. As for the PC cases, the stability is not affected and the maps are virtually identical to the reference case shown in Fig. 4.

As a conclusion, it was shown that pilot hydrogen injection has a strong influence on the stability maps of the present swirl combustor, even at very low flow rates. With 2% of the thermal power from hydrogen, stability is greatly increased for low power operating conditions but degrades for high power. It should be noted that the hydrogen injected in the burner provides only up to 2% of the total power, which is minute. In previous investigations, conducted with fully premixed systems, hydrogen addition between 3.2%–9.1% of the total power was shown to make the system more unstable even at low equivalence ratios [12,14,15]. Comparing between hydrogen injection, methane injection and hydrogen premixing, it can be concluded that for low flow-rates, hydrogen injection is the most efficient method to change the stability characteristics.

## 5. Analysis

In the remainder of this paper, a specific operating point is considered with the objective to explain the mechanism leading to stable operation with pilot hydrogen. It corresponds to  $U_{sw} = 18 \text{ m.s}^{-1}$  and  $\phi_G = 0.80$ . As can be seen by comparing Figs. 4 and 5, this operating point corresponds to a strong instability in the Ref case that is damped with the PH1 and PH2 hydrogen pilot injections.

### 5.1. Pressure traces

Typical pressure and velocity signals recorded during the limit cycle of case Ref (Table 1) are presented in Fig. 8. The traces are all sinusoidal at a frequency  $f = 595 \text{ Hz}$ , despite the large magnitude of the oscillations. The oscillation level reaches around 25% for the heat release rate (HRR) recorded by the PM and 20% for the velocity measured by HW. The RMS of pressure fluctuations recorded by microphone MB at the bottom of the plenum is 1124 Pa. This signal is also in phase with the HRR fluctuations in Fig. 8. Appendix B shows that the acoustic pressure inside the

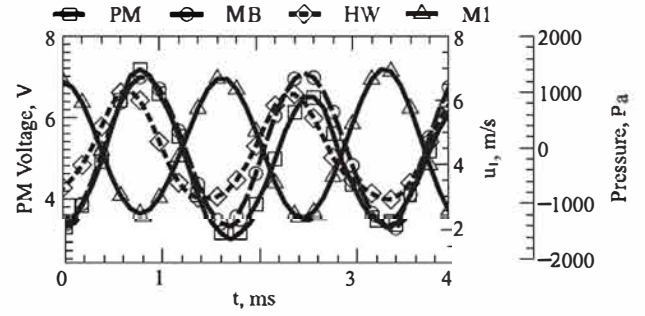


Fig. 8. Pressure (MB, M1), velocity (HW) and heat release rate (PM) time traces for case Ref at  $\phi_G = 0.80$  and  $U_{sw} = 18 \text{ m.s}^{-1}$ .

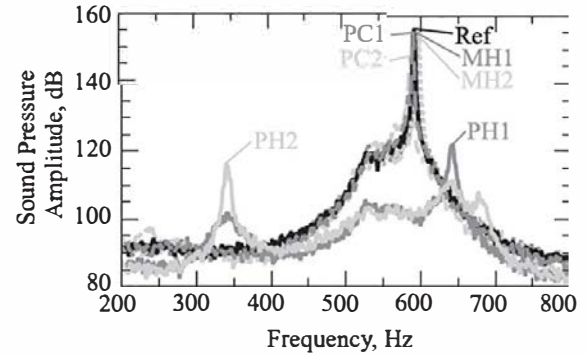


Fig. 9. Power spectra of pressure signals recorded by MB for the cases in Table 1 at  $\phi_G = 0.80$  and  $U_{sw} = 18 \text{ m.s}^{-1}$ .

combustion chamber is also in phase with the pressure recorded by microphone MB.

The fact that the acoustic pressure and the  $\text{CH}^*$  signals remain close to sine waves indicates that the saturation of the system is not due to a redistribution of the acoustic energy into higher harmonics. A full description of mechanisms leading to limit cycle would require to determine the flame describing function for different pulsation levels  $u'_0/\bar{u}_0$ , which is out of the scope of the study. One may however make the following qualitative analysis. The HRR and acoustic pressure inside the chamber being in phase, the Rayleigh index is positive and the instability still feeds acoustic energy in the system at the limit cycle. Therefore saturation is probably due to acoustic fluxes at the boundaries or acoustic losses inside the injector or to a change of the flame response to acoustic disturbances, but the nonlinearity of the flame response remains here weak. It is also worth noting that the pressure traces recorded by microphones MB and M1 are in phase opposition in Fig. 8. An acoustic analysis indicates that the corresponding mode has the structure of a 3/4-wave like mode, featuring at  $f = 591 \text{ Hz}$  a pressure node slightly upstream the section where the signals M1 and HW are recorded. A full characterization of the structure of this mode is given in Appendix B.

The spectra of the pressure signals recorded by microphone MB at the bottom of the plenum are presented in Fig. 9. The most dominant frequencies and their respective amplitudes are listed in Table 2. As expected from the stability maps, the spectra for cases PC and MH are very close to that of the REF case. There is however a notable reduction of the amplitude for PC2 (Table 2), which is coherent with the knowledge that fuel piloting usually damps combustion instabilities. The first remarkable effect of hydrogen injection in the pilot tube (PH cases) is a strong reduction of the peak pressure around 590 Hz. Smaller peaks emerge, at 641 Hz for PH1 and 339 Hz for PH2 but the associated RMS values are low (Table 2) so these conditions are considered stable. These peaks

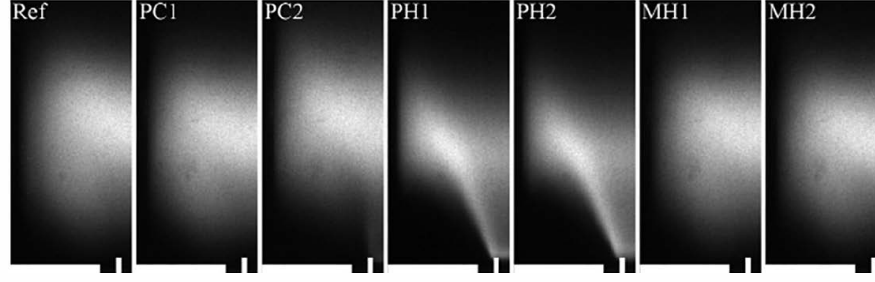


Fig. 10. Flame images with a long chamber and a long plenum for  $\phi_G = 0.80$  and  $U_{sw} = 18 \text{ m.s}^{-1}$  (Table 1). Only the left side of the image with respect the burner axis is presented. The intensity is scaled in order to increase the overall contrast. The location of the burner is added in white at the bottom of each image.

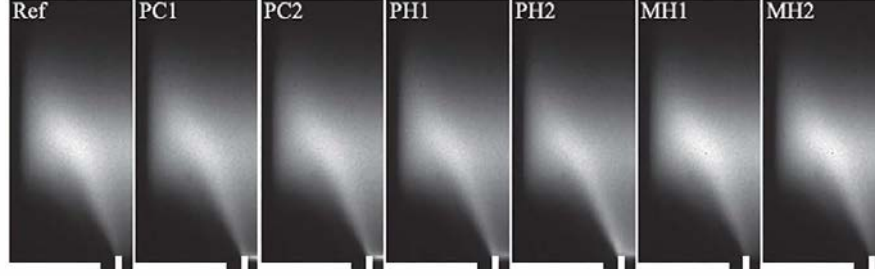


Fig. 11. Flame images with a short combustion chamber and a short plenum for  $\phi_G = 0.80$  and  $U_{sw} = 18 \text{ m.s}^{-1}$  (Table 1). Only the left side image with respect to the burner axis is presented. Camera settings are the identical for all cases meaning that their intensity can be compared. The location of the burner is added in white at the bottom of each image.

Table 2  
Dominant frequencies and corresponding pressure amplitudes for the cases in Table 1 at  $\phi_G = 0.80$  and  $U_{sw} = 18 \text{ m.s}^{-1}$ .

Case	Amplitude, Pa	Frequency, Hz
Ref	1304	591
PH1	25	641
PH2	13	339
PC1	1140	590
PC2	520	586
MH1	1112	596
MH2	1024	597

correspond to acoustic modes of the setup that are excited by the noise from the turbulent flame. Finally, the spectra for the fully premixed (MH) and methane piloting (PC) cases are almost identical to the Ref case.

## 5.2. Direct visualisations

Images of the flames are shown in Fig. 10, corresponding to time-averaged line-of-sight integration of the  $\text{CH}^*$  signal over a long duration. 50 snapshots are taken for each case with a total exposure time of 40 ms. For cases Ref, PC and MH, the  $\text{CH}^*$  signal is spread out over the view frame because of the flame motion associated to the combustion instability. A closer look at PC1 and PC2 however shows that the increase of the methane flow rate slightly enhances the emission of  $\text{CH}^*$  in the wake of the pilot injection tube. For the PH cases, which are stable, the image is much sharper. The two flames are anchored at the outlet of the central pilot tube and there is no obvious difference between  $P_{H_2} = 1\%$  and  $2\%$ .

For a meaningful comparison of the flame shapes and the analysis of the influence of the injection strategies on the flame stabilization, all the cases need to be made stable. This is achieved by changing the acoustic properties of the setup by modifying the lengths of the plenum and flame tube. Experiments are carried out with the short plenum  $l_p = 147 \text{ mm}$  and the short flame tube  $l_f = 100 \text{ mm}$ . Time-averaged images of the  $\text{CH}^*$  signal integrated in the line-of-sight are shown in Fig. 11 for these stable flames.

As expected, all cases are now comparably sharp. The flames are all anchored at the outlet of the central pilot fuel injection tube and the most striking feature is that these flames are very similar at first glance. The shape of the PC, PH and MH flames is almost identical to the Ref case. For the premixed MH cases, this can be explained by the very small increase in the flame speed with hydrogen enrichment. The laminar burning velocity calculated with Cantera and the GRI-mech 3.0 chemistry mechanism is  $S_L = 0.269 \text{ m.s}^{-1}$  for the Ref case and barely increases for MH1 and MH2 cases,  $S_L = 0.275 \text{ m.s}^{-1}$  (+1.6%) and  $S_L = 0.275 \text{ m.s}^{-1}$  (+3.2%), respectively. This is due to the fact that the maximum variation in fuel injection is 2% of the total power corresponding  $X_{H_2}^f = 6.6\%$ .

A closer inspection reveals that the distribution of  $\text{CH}^*$  intensity along the flame arms for the cases with piloting exhibit a more intense  $\text{CH}^*$  emission near the flame base compared to the Ref and MH cases. This zone is more intense for the PC cases than the PH cases, which relates to the fact that hydrogen combustion does not generate  $\text{CH}^*$  radicals.

For a more quantitative evaluation of the changes in flame shape, contours at 35% of the  $\text{CH}^*$  peak intensity are plotted for cases Ref, PH1 and PH2 in Fig. 12. Variations of this threshold level slightly modifies the boundary of these contours, but does not change the difference in flame patterns. The stronger attachment of the flame base is quite obvious but it also appears that the flame height is slightly reduced by the injection of hydrogen. This is a consequence of the increased burning rate when replacing  $\text{CH}_4$  by  $\text{H}_2$  and altogether, these slight modifications of the flame geometry and the redistribution of the volumetric heat release rate through the reaction zone alter the flame response.

## 5.3. Flame Transfer Functions

The forced response of the flames to acoustic excitation is examined by measuring its Flame Transfer Function (FTF):

$$\frac{\tilde{Q}}{\bar{Q}} = G \exp(i\varphi) \frac{\tilde{u}_0}{\bar{u}_0} \quad (5)$$



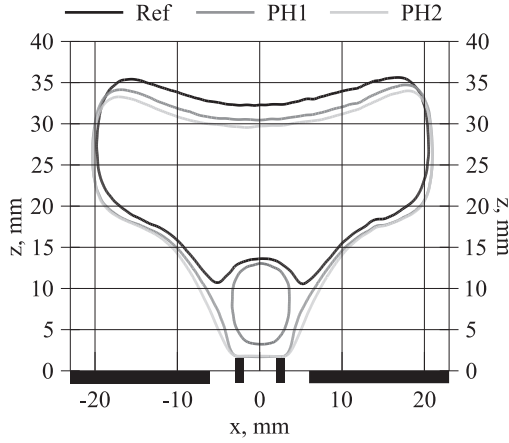


Fig. 12. Contours of 35% of the maximum of  $\text{CH}^*$  intensity from images in Fig. 11.

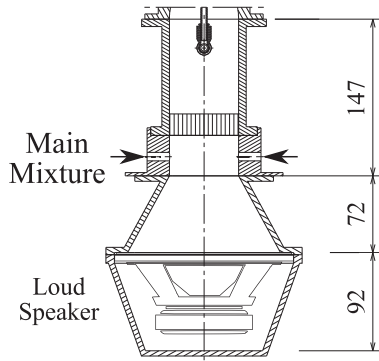


Fig. 13. Schematic representation of the configuration used to measure FTFs.

where  $\dot{Q}$  and  $u_0$  denote the heat release rate and the velocity at the burner outlet in section (0). In this expression,  $\tilde{u}_0$  corresponds to  $U_{sw}$ . The operator  $\tilde{\cdot}$  stands for the Fourier component of the signal at the forcing frequency  $\omega$  and  $\bar{\cdot}$  means the time averaged value. In this framework, the heat release rate fluctuation  $\tilde{\dot{Q}}$ , deduced from the PM equipped with the  $\text{CH}^*$  filter, features a gain  $G$  and a phase lag  $\varphi$  with respect to the acoustic velocity  $\tilde{u}_0$ .

The prerequisite for this task is a stable flame, which is again obtained with the flame tube and plenum lengths  $l_f = 100$  mm and  $l_p = 147$  mm, respectively. In this case the system is void of thermo-acoustic instabilities for all operating points studied. The bottom cap of the plenum is replaced with an extension housing a loudspeaker as shown in Fig. 13. Using this configuration, the flow in the main annular injection channel is submitted to harmonic modulation with a controllable level.

The FTF should be determined with a reference velocity as close as possible to the burner outlet [28]. In a swirling injector, it is difficult to instrument the burner at this location and the technique used in [29] to reconstruct the acoustic velocity  $\tilde{u}_0$  at the burner outlet from the hot wire probe HW and the pressure M1 signals upstream of the swirler is used instead. This is an important aspect of the method because the distance  $l_i = 87$  mm between sections (0) and (1) is not short. Even at relatively low frequencies there may be a node in the acoustic field between HW and the flame. The methodology is fully described in Appendix A.

The forcing by the loudspeaker is tuned so that the amplitude of the velocity fluctuation at the burner outlet is 10% of the bulk velocity for all frequencies  $\tilde{u}_0/U_{sw} = 0.10$ . The resulting FTFs are presented in Fig. 14. For the premixed methane-air Ref case, the flame is very responsive with large FTF gains exceeding unity over almost the entire frequency range explored from 10 Hz to 700 Hz.

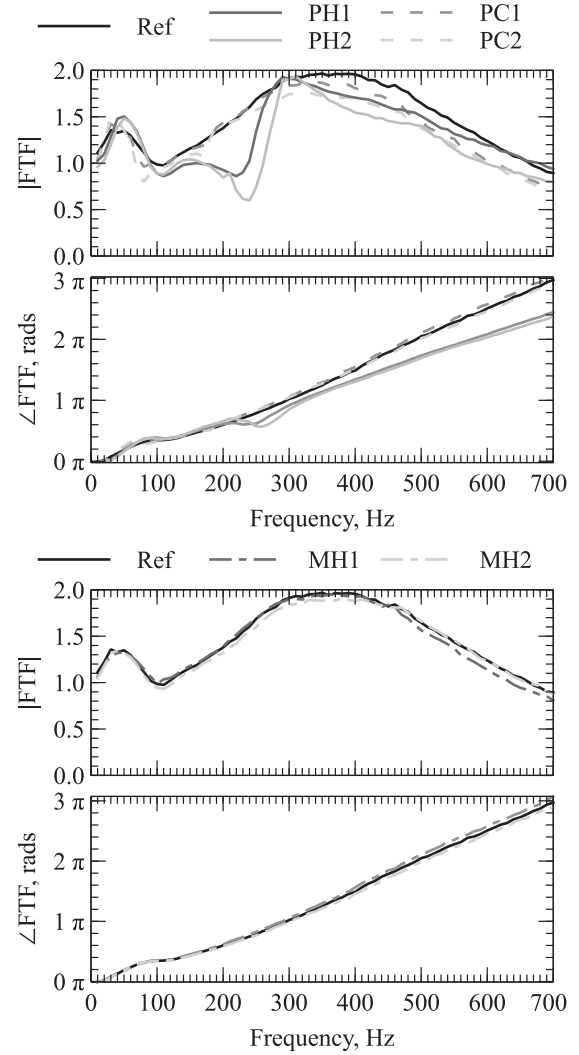


Fig. 14. Flame transfer functions for a constant forcing level  $\tilde{u}_0/U_{sw} = 0.10$  at the burner outlet.

Regarding the fully premixed MH cases, hydrogen addition in the fuel at such low concentration levels does not impact the flame response in Fig. 14. This observation is consistent with the stability maps and the flame visualizations. A fuel blend with a few percent of hydrogen,  $X_{H_2}^f < 7\%$  does not alter the dynamic stability of the system. The laminar burning velocity was already shown to change less than 3.3% for MH2. Changes of the adiabatic flame temperature for mixtures Ref, MH1 and MH2 are also smaller than 1%.

Methane injection in the central pilot fuel line corresponding to cases PC1 and PC2 has more effect and visibly decreases the FTF gain  $G$  for frequencies higher than 250 Hz in Fig. 14. The FTF phase lag  $\varphi$  is marginally altered. The Rayleigh index, that has been shown to take a positive value for the Ref case at this operating condition, remains positive for PC1 and PC2 because the FTF phase lag is identical for the Ref case and the PC cases. The small drop in the FTF gain around 600 Hz is consistent with the modest reduction of the limit-cycle amplitude of the unstable mode observed for the PC cases in Fig. 9 (see also Table 2). For case PC2, there is a small bump in the FTF gain at 30 Hz followed by a dip at 80 Hz, but these features are not explained.

The strongest alteration of the FTF is obtained with hydrogen piloting for cases PH1 and PH2. The most obvious impact is the large reduction of the FTF gain in the range 150–300 Hz, which is more pronounced for PH2 than PH1 when the hydrogen flowrate

**Table 3**CO and NOx emissions measured at the flame tube outlet for  $U_{sw}=18 \text{ m.s}^{-1}$  and  $\phi=0.8$ .

ppm	Ref	PH1	PH2	MH1	MH2	PC1	PC2
NOx	$12.4 \pm 0.6$	$14.4 \pm 0.7$	$15.6 \pm 0.8$	$12.8 \pm 0.6$	$12.8 \pm 0.6$	$13.8 \pm 0.7$	$14.1 \pm 0.7$
CO	$10.0 \pm 1$	$10.0 \pm 1$	$9.0 \pm 1$	$10.0 \pm 1$	$10.0 \pm 1$	$10.0 \pm 1$	$10.0 \pm 1$

is increased. This could be an effective control strategy but at this operating point, the instability is not in this frequency range. The large dip of the gain  $G$  around 220–240 Hz with a change in the slope of the phase lag  $\varphi$  is characteristic of interferences between acoustic waves and azimuthal convective waves downstream the swirler [25,30,31]. This feature is not discussed here since our focus is on the influence of piloting and hydrogen addition. The scrutiny of this mechanism is left to further studies.

Above 300 Hz, the FTF gain for the PH cases lies below the Ref case in Fig. 14, but the difference is not sufficient to explain the difference in stability. For frequencies higher than 300 Hz, the FTF phase lags between the PH and Ref cases begin to deviate and the difference increases with the forcing frequency, resulting in a large difference at the frequency of the instability. Around 590 Hz, one reads in Fig. 14:  $\varphi(590) \sim 7.75$  rad for the Ref, PC1, PC2, MH1 and MH2 cases and  $\varphi(590) = 6.36$  rad for the PH1 and PH2 cases.

This large difference of the FTF phase lag  $\varphi$  is at the origin of the augmented stability margins of the PH cases. This is highlighted by conducting a simplified acoustic energy balance. For a compact flame, the thermo-acoustic energy release at frequency  $f = 1/T$  in the system is determined by the Rayleigh index:

$$\mathcal{R} = \frac{1}{T} \int_T \frac{\gamma - 1}{\gamma \bar{p}} p' \dot{Q}' dt = \frac{\gamma - 1}{2\gamma \bar{p}} \text{Re} \left[ Z \tilde{u}_0 \tilde{Q}^* \right] \quad (6)$$

In this expression  $\text{Re}[\cdot]$  is the real component of the complex argument and the star denotes the complex conjugate. It makes use of the complex burner impedance  $Z$  at the instability frequency  $f$ :

$$Z = \frac{\tilde{p}_0}{\tilde{u}_0} = |Z| \exp(i\varphi_0) \quad (7)$$

where  $\tilde{p}_0$  and  $\tilde{u}_0$  denote the acoustic pressure and velocity at the burner outlet in section (0). In this study, the phase lag  $\varphi_0$  in section (0) is deduced from reconstructions of  $\tilde{p}_0$  and  $\tilde{u}_0$  with measurements of  $\tilde{p}_1$  and  $\tilde{u}_1$  made in section (1). This reconstruction of the acoustic field at the burner outlet was verified with pressure measurements taken from inside the chamber as explained in Appendix B.

When the Rayleigh index is positive  $\mathcal{R} > 0$  the combustion dynamics destabilizes the system. When  $\mathcal{R} < 0$ , the flame damps acoustic perturbations and the system is stable. Eqs. (5) and (7) are used to rewrite the Rayleigh source term as a function of the phase lags from the burner impedance  $Z$  and FTF:

$$\mathcal{R} = \frac{(\gamma - 1)\bar{Q}}{2\gamma \bar{p} U_{sw}} |\tilde{u}_0|^2 |Z| G \cos(\varphi_0 - \varphi) \quad (8)$$

When the burner impedance  $Z$ , the FTF or the acoustic velocity  $\tilde{u}_0$  at the burner outlet vanishes, there is no thermo-acoustic energy release  $\mathcal{R} = 0$ . For all other conditions, the thermo-acoustic source may damp  $\mathcal{R} < 0$  or amplify  $\mathcal{R} > 0$  acoustic perturbations, depending on the phase lags  $\varphi_0$  and  $\varphi$  from the burner impedance  $Z$  and FTF, respectively. According to Eq. (8) and neglecting other damping mechanisms, unstable modes need to comply with:

$$-\frac{\pi}{2} [2\pi] < \varphi - \varphi_0 < \frac{\pi}{2} [2\pi] \quad (9)$$

Knowing that the burner impedance at  $f \approx 590$  Hz is  $\varphi_0 \approx 1.96$  rad, one deduces that to trigger an instability the FTF phase lag necessarily belongs to:

$$0.39 < \varphi < 3.53 \quad \text{or} \quad 6.67 < \varphi < 9.82 \quad (10)$$

For the REF methane/air case, methane piloting PC1 and PC2 cases and the fully premixed hydrogen/methane MH1 and MH2 cases, the FTF phase lag  $\varphi(590) \sim 7.69$  rad falls within the second instability region. With hydrogen piloting, PH1 and PH2,  $\varphi(590) \sim 6.36$  rad falls within the stable band  $3.53 < \varphi < 6.67$ .

This analysis shows that minimal hydrogen injection through a pilot jet is an efficient way to alter the FTF with significant changes of the gain at low forcing frequencies and phase lag at high forcing frequencies. This in turn can be used to drastically change the stability margins of the combustor.

Experiments, not shown here, have also been repeated by replacing the  $\text{CH}^*$  filter by an  $\text{OH}^*$  filter to deduce the heat release rate fluctuations. It was found that the measured FTF is independent of the selected filter to deduce heat release rate fluctuations for all injection strategies tested (PM, PH and PC) with  $P_{H_2}=1\%$  and  $2\%$ .

## 6. Emissions

Another aspect that needs to be considered is the pollutant emissions. NOx emissions are a known issue for hydrogen enriched flames. CO and NOx concentration measurements in the burnt gases have been performed with a gas analyzer ECOM J2KN PRO by probing the flow at the outlet of a 200 mm length combustion chamber. Care has been taken to prevent combustion products mixing with the ambient air. Results for  $U_{sw}=18 \text{ m.s}^{-1}$  and  $\phi=0.8$  and the different injection strategies are presented in Table 3.

Injection of hydrogen premixed with the main methane/air mixture does not modify emissions for the MH cases. Methane and hydrogen piloting do not alter CO emissions, but they increase NOx emissions even for these small flowrates. PC2 and PH2 injection strategies with only 2% of the power originating from combustion of the pilot fuel, lead to an increase of NOx concentrations in the flue gases of +16% for methane and +25% for hydrogen injection. These results put in forward that an optimization needs to be performed between the benefits of the change in the FTF obtained from the injection of hydrogen, and the increase of NOx emissions coming from the non-premixed part of the flame when pure hydrogen is injected.

## 7. Conclusion

In this work, the control of combustion instabilities via separate hydrogen injection was studied. The configuration is a swirled premixed methane/air burner, tested over a wide range of operating conditions through variations of bulk flow velocity and equivalence ratio. The goal was to assess control strategies that would require very low fractions of hydrogen, therefore the maximum investigated is 2% of the thermal power. For each operating condition, the air flow rate and total thermal power are kept constant. The reference being the fully premixed methane case, three alternatives are considered: pilot injection of hydrogen (PH), pilot injection of methane (PC) and fully premixed methane hydrogen (MH). These allow to discriminate between fuel composition effects and injection strategies.

The analysis of stability maps, pressure traces, flame images and Flame Transfer Functions led to the following conclusions:

1. When the hydrogen is fully premixed with methane and air the stability map is not affected.
2. Pilot injection of pure hydrogen strongly affects the stability map with a significant reduction of the unstable zones.
3. Classical pilot injection of methane has a weak stabilizing effect at such low fraction of the total power ( $< 2\%$ ).
4. Piloting with hydrogen affects the flame anchoring resulting in slightly shorter flames with a redistribution of the volumetric heat release toward the bottom of the flame.
5. Both the gain and phase lag of the FTF are massively affected by pilot hydrogen addition with different behaviors depending on the frequency range.
6. NOx emissions need to be monitored to select the best compromise between augmented stability margins and reduced emission levels.

It is concluded that hydrogen injection can be used as an efficient passive control means to mitigate thermo-acoustic instabilities. Small changes in the percentage of hydrogen addition result in stable regimes, otherwise unstable without injection for the same thermal power and air flow rate. This effect is more pronounced at low power regimes, resulting in a system that has augmented stability margins.

### Declaration of Competing Interest

We, the authors, declare that we have no known competing financial interests or personal relationships that could have appeared to influence the work reported in this paper.

### Acknowledgments

The research leading to these results has received funding from the [European Research Council](#) under the European Union's Seventh Framework Programme (FP/2007-2013)/ERC Grant Agreement [ERC-AdG 319067-INTECOIS](#).

### Appendix A. Methodology for FTF reconstruction

The method developed in [29] is used to infer the FTF at the burner outlet in section (0) from measurements of the acoustic velocity  $\tilde{u}_1$  and pressure  $\tilde{p}_1$  with HW and M1 in section (1) below the swirling vane. In section (1), the flow is laminar with a top hat velocity profile. The velocity  $\tilde{u}_0$  at the burner outlet differs from  $\tilde{u}_1$  because the distance  $l_i = 87$  mm between sections (0) and (1) is quite large and the burner is not compact for the range of frequencies of interest  $0 \leq f \leq 700$  Hz. At  $f = 700$  Hz,  $He = 2\pi f l_i / c \sim 1$ . The method is based on the low order model of the burner cavities presented in Fig. 15.

At low harmonic forcing frequencies, the acoustic field inside the combustor cavities can be assumed to be 1D and can be represented by the complex amplitudes  $A^+$  and  $A^-$  of upstream and downstream waves in each cavity. For an harmonic perturbation in the Fourier space at angular frequency  $\omega$ ,  $a' = \text{Re } \tilde{a} e^{-i\omega t}$ , one has along the burner  $z$ -axis:

$$\tilde{p}_j = A_j^+ e^{ik_j z} + A_j^- e^{-ik_j z} \quad (\text{A.1})$$

and

$$\rho_j c_j \tilde{u}_j = A_j^+ e^{ik_j z} - A_j^- e^{-ik_j z} \quad (\text{A.2})$$

where  $k_j = \omega / c_j$  is the wave number,  $c_j$  the speed of sound,  $\rho_j$  the density of the medium and  $z_j$  is the position in the  $j$ th section. As the sound speed and density do not change in the sections considered, the subscripts are removed. With these complex wave amplitudes, the acoustic pressure  $\tilde{p}_j$  and acoustic velocity  $\tilde{u}_j$  at any section  $S_j$  of the combustor can be reconstructed.

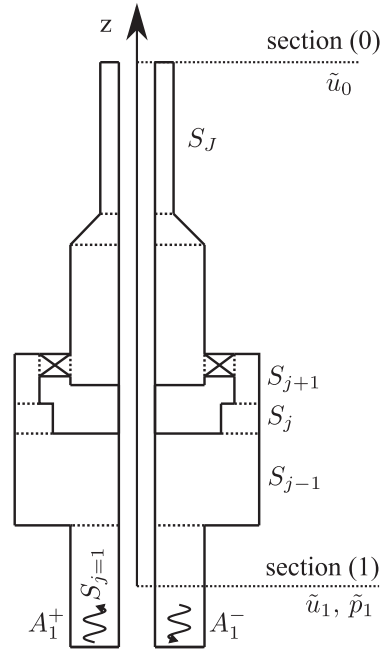


Fig. 15. Schematic representation of acoustic reconstruction through the different sections of the swirled injector.

The wave amplitudes  $A_1^+$  and  $A_1^-$  in section (1) are determined from the microphone M1 and HW measurements:

$$A_1^+ e^{ik_1 z_1} + A_1^- e^{-ik_1 z_1} = \tilde{p}_1 \quad (\text{A.3})$$

$$A_1^+ e^{ik_1 z_1} - A_1^- e^{-ik_1 z_1} = \rho c \tilde{u}_1 \quad (\text{A.4})$$

where  $\tilde{p}_1$  and  $\tilde{u}_1$  are the Fourier components of the pressure and velocity signals evaluated at the forcing frequency  $f$  respectively. This linear system of equations is solved for  $A_1^+$  and  $A_1^-$ . Subsequently, using continuity of acoustic pressure and of acoustic volumetric flow rate, the jump conditions at abrupt section changes are given by [32]:

$$\tilde{p}_j(z_{j+1}) = \tilde{p}_{j+1}(z_{j+1}) \quad (\text{A.5})$$

$$S_j \tilde{u}_j(z_{j+1}) = S_{j+1} \tilde{u}_{j+1}(z_{j+1}) \quad (\text{A.6})$$

where  $l_j$  is the length and  $S_j$  is the cross-sectional area of the  $j$ th section. With these relations the transfer matrix relating the wave amplitudes of the subsequent sections can be constructed as:

$$\begin{bmatrix} A_{j+1}^+ \\ A_{j+1}^- \end{bmatrix} = T_j \begin{bmatrix} A_j^+ \\ A_j^- \end{bmatrix} \quad (\text{A.7})$$

where  $T_j$  is defined as:

$$T_j = \frac{1}{2} \begin{bmatrix} e^{ik_j l_j} (1 + \Gamma) & e^{-ik_j l_j} (1 - \Gamma) \\ e^{ik_j l_j} (1 - \Gamma) & e^{-ik_j l_j} (1 + \Gamma) \end{bmatrix} \quad (\text{A.8})$$

and  $\Gamma = S_j / S_{j+1}$ . A global matrix relating any two sections connected with multiple sections in between can be constructed. These relations are used to calculate the complex wave amplitudes in the main annular injection channel as:

$$\begin{bmatrix} A_0^+ \\ A_0^- \end{bmatrix} = M \begin{bmatrix} A_1^+ \\ A_1^- \end{bmatrix} \quad (\text{A.9})$$

where  $M$  is the global transfer matrix cast as:

$$M = \prod_{j=1}^{J-1} T_j \quad (\text{A.10})$$

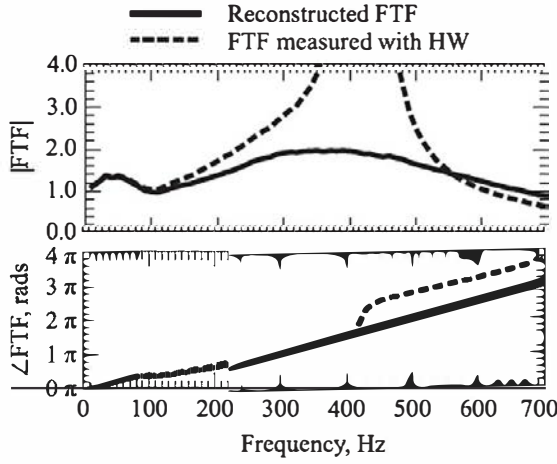


Fig. 16. FTF for the Ref case. The dotted line is the FTF determined with the HW signal measured in section (1). The straight line is the FTF using the reconstructed velocity  $u'_0$  at the burner outlet in section (0) from the low order model and the HW and M1 signals.

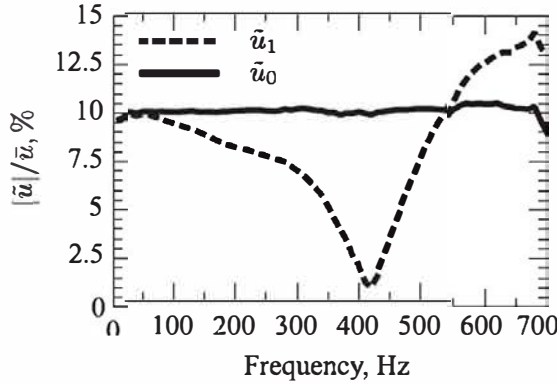


Fig. 17. Velocity fluctuation level in sections (1) and (0) used for the FTF determination. The operator  $\tilde{\cdot}$  denotes here the bulk flow velocity in the corresponding section.

where  $j = 1$  stands for the HW duct and  $j - 1$  denotes the duct just before the injector annular channel. After the wave amplitudes at the main annular injection channel are determined, the acoustic velocity  $\tilde{u}_0$  at the burner outlet in section (0) corresponds to:

$$\tilde{u}_0 = A_n^+ + A_n^- \quad (\text{A.11})$$

The FTF is deduced from the light intensity  $I$  from CH\* radicals recorded by the PM and the velocity  $u_0$  at the burner outlet:

$$FTF = \frac{\tilde{I} U_{sw}}{\tilde{I} \tilde{u}_0} = G(f, |\tilde{u}_0/U_{sw}|) e^{i\varphi(f, |\tilde{u}_0/U_{sw}|)} \quad (\text{A.12})$$

Figure 16 compares the FTF determined with the reference signals  $\tilde{u}_0$  and  $\tilde{u}_1$ . The FTF deduced from the hot wire measurements in section (1) is obviously incorrect. The hot wire lies 87 mm below the burner outlet leading to different acoustic velocity fluctuations at the outlet of the main annular injection channel and the channel where the HW is located. There is also a velocity node near the HW position when the system is pulsated at 420 Hz and the FTF gain determined with HW diverges around this forcing frequency.

Another important feature when determining the FTF is to keep the same forcing level at the burner outlet [33]. An iterative algorithm was developed to keep this perturbation level equal to  $\tilde{u}_0/U_{sw} = 0.10$ . The difference between the velocity fluctuation amplitude recorded with the hot wire HW in section (1) and the reconstructed velocity amplitude  $|\tilde{u}_0|$  in section (0) is presented in

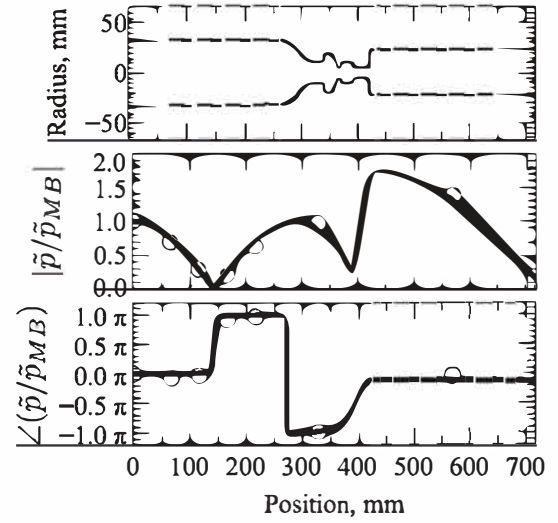


Fig. 18. Comparison between measurements (circles) and predictions (full line) of the acoustic pressure distribution along the combustor of the unstable mode calculated with OSCILOS (<http://www.oscilos.com>).

Fig. 17. This last test validates the FTF reconstruction technique and the results shown in Fig. 14.

## Appendix B. Acoustic Structure of the Mode

A low order thermo-acoustic model of the combustor has been constructed with the help of the OSCILOS simulator [34]. This model includes the flame response with the gain and the phase lag measured at the limit cycle of the Ref case. The reflection coefficient at the inlet has been taken to be a fully reflecting velocity node. The outlet of the combustion chamber exhausting burnt gases is open to atmosphere. Measurements of the outlet reflection coefficient in hot conditions were made and a fit was included in the numerical model. The temperature at the outlet of the 300 mm combustion chamber has been measured with a thermocouple. Temperature measurements corrected for thermal radiation were used to calculate the speed of sound and density in the flame tube. The fresh mixture in the plenum is at ambient conditions. The structure of the instability observed for the Ref case at  $U_{sw} = 18 \text{ m.s}^{-1}$  and  $\phi = 0.8$  is presented in Fig. 18. The top image shows a schematic of the burner cavities. The middle plot shows the pressure amplitude with respect to that measured by microphone MB at the bottom of the plenum. The bottom plot shows the phase lag with respect to that measured by microphone MB. This figure confirms that the acoustic pressure in the flame tube is in phase with the pressure signal measured by microphone MB.

## References

- [1] P. Jaramillo, W.M. Griffin, H.S. Matthews, Comparative life-cycle air emissions of coal, domestic natural gas, LNG, and SNG for electricity generation, *Environ. Sci. Technol.* 41 (17) (2007) 6290–6296.
- [2] P. Viebahn, J. Mitsch, M. Fischedick, A. Esken, D. Schüwer, N. Supersberger, U. Zuberbühler, O. Edenhofer, Comparison of carbon capture and storage with renewable energy technologies regarding structural, economic, and ecological aspects in germany, *Int. J. Greenh. Gas Control* 1 (1) (2007) 121–133.
- [3] N.A. Odeh, T.T. Cockerill, Life cycle GHG assessment of fossil fuel power plants with carbon capture and storage, *Energy Policy* 36 (1) (2008) 367–380.
- [4] T. Poinso, Prediction and control of combustion instabilities in real engines, *Proc. Combust. Inst.* 36 (1) (2017) 1–28.
- [5] T.C. Lieuwen, V. Yang, Combustion instabilities in gas turbine engines: operational experience, fundamental mechanisms and modeling, *Progress in Astronautics and Aeronautics*, American Institute of Aeronautics and Astronautics (2005).
- [6] R.L. Speth, A.F. Ghoniem, Using a strained flame model to collapse dynamic mode data in a swirl-stabilized syngas combustor, *Proc. Combust. Inst.* 32 (2) (2009) 2993–3000.



- [7] K. Liu, V. Sanderson, The influence of changes in fuel calorific value to combustion performance for siemens SGT-300 dry low emission combustion system, *Fuel* 103 (2013) 239–246.
- [8] C.J. Mordaunt, W.C. Pierce, Design and preliminary results of an atmospheric-pressure model gas turbine combustor utilizing varying CO<sub>2</sub> doping concentration in CH<sub>4</sub> to emulate biogas combustion, *Fuel* 124 (2014) 258–268.
- [9] T. García-Armingol, J. Ballester, Operational issues in premixed combustion of hydrogen-enriched and syngas fuels, *Int. J. Hydrogen Energy* 40 (2) (2015) 1229–1243.
- [10] P. Jansohn (Ed.), *Modern gas turbine systems: high efficiency, low emission, fuel flexible power generation*, Woodhead publishing, 2013.
- [11] R.W. Schefer, D.M. Wicksall, A.K. Agrawal, Combustion of hydrogen-enriched methane in a lean premixed swirl-stabilized burner, *Proc. Combust. Inst.* 29 (1) (2002) 843–851.
- [12] L. Figura, J.G. Lee, B.D. Quay, D.A. Santavicca, The effects of fuel composition on flame structure and combustion dynamics in a lean premixed combustor, GT2007-27298, ASME Turbo Expo, May 14–17, 2007 Montreal, Canada, no. 47918 (2007), pp. 181–187.
- [13] D.M. Wicksall, A.K. Agrawal, Acoustics measurements in a lean premixed combustor operated on hydrogen/hydrocarbon fuel mixtures, *Int. J. Hydrogen Energy* 32 (8) (2007) 1103–1112.
- [14] S. Taamallah, K. Vogiatzaki, F.M. Alzahrani, E.M.A. Mokheimer, M.A. Habib, A.F. Ghoniem, Fuel flexibility, stability and emissions in premixed hydrogen-rich gas turbine combustion: Technology, fundamentals, and numerical simulations, *Appl. Energy* 154 (2015) 1020–1047.
- [15] S. Taamallah, Z.A. LaBry, S.J. Shanbhogue, A.F. Ghoniem, Thermo-acoustic instabilities in lean premixed swirl-stabilized combustion and their link to acoustically coupled and decoupled flame macrostructures, *Proc. Combust. Inst.* 35 (3) (2015) 3273–3282.
- [16] G.A. Richards, R.S. Gemmen, M.J. Yip, A test device for premixed gas turbine combustion oscillations, *J. Eng. Gas Turb. Power* 119 (4) (1997) 776–782.
- [17] D.W. Kendrick, T.J. Anderson, W.A. Sowa, T.S. Snyder, Acoustic sensitivities of lean-premixed fuel injectors in a single nozzle rig, *J. Eng. Gas Turb. Power* 121 (3) (1999) 429–436.
- [18] K.O. Smith, D.C. Rawlins, R.C. Steele, Developments in dry low emissions systems, 3rd International Pipeline Conference, October 1–5, 2000, Calgary, Alberta, Canada, no. 40252 (2000). p. V002T09A010
- [19] R.C. Steele, L.H. Cowell, S.M. Cannon, C.E. Smith, Passive control of combustion instability in lean premixed combustors, *J. Eng. Gas Turb. Power* 122 (3) (2000) 412–419.
- [20] C.J. Etheridge, Mars soloNOx: Lean premix combustion technology in production, in: 94-GT-255, ASME Turbo Expo 1994, June 13–16, 1994 The Hague, Netherlands, no. 78859 (1994). p. V003T06A013.
- [21] C.O. Paschereit, P. Flohr, H. Knopfel, W. Geng, C. Steinbach, P. Stuber, K. Bengtsson, E. Gutmark, Combustion control by extended EV burner fuel lance, in: GT2002-30462, ASME Turbo Expo 2002, June 3–6, 2002 Amsterdam, the Netherlands, no. 36061 (2002), pp. 721–730.
- [22] T. Hussain, M. Talibi, R. Balachandran, Investigating the effect of local addition of hydrogen to acoustically excited ethylene and methane flames, *Int. J. Hydrogen Energy* 44 (21) (2019) 11168–11184.
- [23] D.N. Anderson, Effect of hydrogen injection stability and emissions of an experimental premixed prevaporized propane burner, in: Nasa Technical Memorandum, NASATM X-3301.
- [24] S. Barbosa, M. de La Cruz Garcia, S. Ducruix, B. Labegorre, F. Lacas, Control of combustion instabilities by local injection of hydrogen, *Proc. Combust. Inst.* 31 (2) (2007) 3207–3214.
- [25] P. Palies, D. Durox, T. Schuller, S. Candel, The combined dynamics of swirler and turbulent premixed swirling flames, *Combust. Flame* 157 (9) (2010) 1698–1717.
- [26] D. Durox, J.P. Moeck, J.-F. Bourgoign, P. Morenton, M. Viallon, T. Schuller, S. Candel, Flame dynamics of a variable swirl number system and instability control, *Combust. Flame* 160 (9) (2013) 1729–1742.
- [27] M. Gatti, R. Gaudron, C. Mirat, L. Zimmer, T. Schuller, Impact of swirl and bluff-body on the transfer function of premixed flames, *Proc. Combust. Inst.* 37 (4) (2019) 5197–5204.
- [28] K. Truffin, T. Poinot, Comparison and extension of methods for acoustic identification of burners, *Combust. Flame* 142 (4) (2005) 388–400.
- [29] R. Gaudron, M. Gatti, C. Mirat, T. Schuller, Flame describing functions of a confined premixed swirled combustor with upstream and downstream forcing, *J. Eng. Gas Turb. Power* 141 (5) (2019) 51016–51019.
- [30] T. Komarek, W. Polifke, Impact of swirl fluctuations on the flame response of a perfectly premixed swirl burner, *J. Eng. Gas Turb. Power* 132 (6) (2010) 061503.
- [31] N.A. Bunce, B.D. Quay, D.A. Santavicca, Interaction between swirl number fluctuations and vortex shedding in a single-nozzle turbulent swirling fully-premixed combustor, *J. Eng. Gas Turb. Power* 136 (2) (2013) 021503.
- [32] T. Poinot, D. Veynante, *Theoretical and Numerical Combustion*, CNRS, 2011.
- [33] D. Durox, T. Schuller, N. Noiray, S. Candel, Experimental analysis of nonlinear flame transfer functions for different flame geometries, *Proc. Combust. Inst.* 32 (1) (2009) 1391–1398.
- [34] X. Han, J. Li, A.S. Morgans, Prediction of combustion instability limit cycle oscillations by combining flame describing function simulations with a thermoacoustic network model, *Combust. Flame* 162 (10) (2015) 3632–3647.